Interannual Variability in Sea Surface Height at Southern Midlatitudes of the Indian Ocean

MOTOKI NAGURA[a] AND MICHAEL J. MCPHADEN[b]

[a] *Japan Agency for Marine-Earth Science and Technology, Yokosuka, Kanagawa, Japan*
[b] *National Oceanic and Atmospheric Administration/Pacific Marine Environmental Laboratory, Seattle, Washington*

(Manuscript received 6 November 2020, in final form 27 January 2021)

ABSTRACT: This study examines interannual variability in sea surface height (SSH) at southern midlatitudes of the Indian Ocean (10°–35°S). Our focus is on the relative role of local wind forcing and remote forcing from the equatorial Pacific Ocean. We use satellite altimetry measurements, an atmospheric reanalysis, and a one-dimensional wave model tuned to simulate observed SSH anomalies. The model solution is decomposed into the part driven by local winds and that driven by SSH variability radiated from the western coast of Australia. Results show that variability radiated from the Australian coast is larger in amplitude than variability driven by local winds in the central and eastern parts of the south Indian Ocean at midlatitudes (between 19° and 33°S), whereas the influence from eastern boundary forcing is confined to the eastern basin at lower latitudes (10° and 17°S). The relative importance of eastern boundary forcing at midlatitudes is due to the weakness of wind stress curl anomalies in the interior of the south Indian Ocean. Our analysis further suggests that SSH variability along the west coast of Australia originates from remote wind forcing in the tropical Pacific, as is pointed out by previous studies. The zonal gradient of SSH between the western and eastern parts of the south Indian Ocean is also mostly controlled by variability radiated from the Australian coast, indicating that interannual variability in meridional geostrophic transport is driven principally by Pacific winds.

SIGNIFICANCE STATEMENT: A complete understanding of climate variability and change requires knowledge of the interactions between ocean basins on interannual to decadal time scales. In this study, we examined the cause of sea level variability in the south Indian Ocean and its connection with variability in the Pacific Ocean, using satellite observations and a one-dimensional wave model. We found that sea level variability at midlatitudes of the south Indian Ocean is mainly driven by El Niño–Southern Oscillation (ENSO). Surface wind anomalies associated with ENSO excite sea level variations in the Pacific Ocean, which propagates into the western coast of Australia through the Indonesian Archipelago and then into the interior of the south Indian Ocean. This study emphasizes the importance of connectivity via the oceanic route to understand midlatitude circulation variability in the south Indian Ocean.

KEYWORDS: Ocean; Indian Ocean; Ocean dynamics; Rossby waves; Interannual variability

1. Introduction

In the south Indian Ocean, the westward South Equatorial Current is evident north of about 20°S, and an anticyclonic subtropical gyre is located between 15° and 40°S (Stramma and Lutjeharms 1997; Nagura and McPhaden 2018). Many previous studies reported interannual to decadal time scale variability in sea surface height (SSH) and thermocline depth at latitudes where the South Equatorial Current is present (e.g., Han et al. 2014, and references therein). Some of these studies attributed this variability to local wind forcing (Masumoto and Meyers 1998; Trenary and Han 2008), but many others argued for the importance of remote forcing from the Pacific Ocean. In particular, SSH variability in the tropical Pacific Ocean can propagate into the south Indian Ocean through the Indonesian Archipelago and along the west coast of Australia (Clarke 1991; Clarke and Liu 1994; Feng et al. 2010, 2011; Menezes and Vianna 2019; Meyers 1996; Potemra 2001; Wijffels and Meyers 2004). This SSH variability along the eastern boundary then propagates to the west as a long Rossby wave to affect SSH in the interior ocean. This oceanic connection between the Pacific and Indian basins contributes to the generation of interannual to decadal climate variability at low latitudes of the south Indian Ocean. For example, Lee et al. (2015), Nieves et al. (2015), and Vialard (2015) reported that heat content in the upper ocean was shifted from the Pacific to the Indian Ocean during the recent hiatus in global warming. Feng et al. (2013) and Kataoka et al. (2014) pointed out that El Niño–Southern Oscillation (ENSO) in the Pacific Ocean excites interannual variability in SSH and sea surface temperature (SST) off northwest of Australia, which is referred to as Ningaloo Niño or Niña depending on sign, via the propagation of SSH anomalies through the Indonesian Archipelago.

Relatively few studies, on the other hand, have examined variability at midlatitudes of the south Indian Ocean. Lee (2004), Lee and McPhaden (2008), Zhuang et al. (2013), and Nagura (2020) reported interannual to decadal variability in the zonal gradient of SSH anomalies between the western and eastern parts of the south Indian Ocean, which represents variability in zonally integrated meridional geostrophic transport. Menezes and Vianna (2019) also examined zonal propagation of SSH anomalies at midlatitudes in the south Indian Ocean, while Volkov et al. (2020) studied variability in SSH and heat content averaged over the south Indian Ocean.

The dynamics of interannual/decadal variability in SSH at midlatitudes of the south Indian Ocean, however, has not been

Corresponding author: Motoki Nagura, nagura@jamstec.go.jp

DOI: 10.1175/JPO-D-20-0279.1

fully investigated, particularly with regard to the role of Indo-Pacific connectivity and the relative importance of local and remote wind forcing. SSH variability in the south Indian Ocean can be driven both by local wind forcing and by wind forcing from the Pacific Ocean, the latter of which is through the Indonesian Archipelago, poleward propagation of coastal Kelvin waves along the western Australian coast and subsequent westward propagation into the interior as long Rossby waves. Previous studies examined the relative effectiveness of local and remote forcing. Zhuang et al. (2013) and Menezes and Vianna (2019) argued that SSH variability along 20° and 25°S, respectively, is mainly driven by variability radiated from the eastern boundary, with a secondary contribution from local wind forcing. Masumoto and Meyers (1998) and Zhuang et al. (2013) on the other hand reported that local wind forcing is the primary forcing of SSH variability at lower latitudes (11°–13°S), suggesting that the relative importance of remote and local forcing depends on latitude. Moreover, Volkov et al. (2020) pointed out that SSH variability in the eastern basin is mainly driven by variability radiated from the eastern boundary, whereas that in the western basin is more influenced by local wind forcing, indicating a dependence on longitude. They also reported that the relative importance of local and remote forcing changes from period to period with, for example, a dominance of local wind forcing in 2017–18, during which basin-averaged SSH rapidly increased. However, Volkov et al. examined SSH variability averaged over 10°–30°S, from which latitudinal dependence was not resolved.

To fully describe the contributions from local and remote forcing to SSH variability in the south Indian Ocean, we conduct a comprehensive analysis spanning tropical latitudes (10°S) to the southern tip of the Australian continent (35°S). We use a linear, one-dimensional (1D), 1.5-layer long Rossby wave model and separate SSH variability into the part that is driven by local winds and that driven by SSH variability radiated from the eastern boundary. We compare the two components and show that the dominant dynamics differs depending on latitude as well as on longitude (i.e., the western versus eastern halves of the basin). The remainder of this paper is organized as follows. Section 2 describes used datasets, the model and parameter choices. Section 3 presents results, and section 4 adds perspective on the interpretation of those results. Finally, section 5 provides a summary of our main conclusions.

2. Data and model

We obtained monthly averages of SSH anomalies from satellite altimetry provided by the Copernicus Marine and Environment Monitoring Service (CMEMS; Ducet et al. 2000). The horizontal grid spacings of SSH data are 0.25° in longitude and latitude. Global mean of SSH increases over the period of satellite altimetry observations (Church and White 2006), so we subtracted the global mean of SSH from monthly SSH maps to focus on interannual variations. Surface wind stresses and sea level pressure (SLP) were obtained from ECMWF reanalysis 5 (ERA5; Hersbach et al. 2020). The grid intervals are 0.25° × 0.25°, and monthly averages were used. A 13-month running mean filter was applied to smooth out seasonal cycles. Monthly averages of SST were obtained from National Oceanic and Atmospheric Administration (NOAA) Optimum Interpolation (OI) SST V2 (Reynolds et al. 2002), which is on a 1° × 1° grid.

The linear, 1D, 1.5-layer long Rossby wave model was widely used by previous studies for the examination of SSH variability (e.g., Qiu and Chen 2006; Zhuang et al. 2013; Menezes and Vianna 2019; Volkov et al. 2020). This model is formulated as (e.g., Qiu et al. 1997)

$$\frac{\partial \eta}{\partial t} - c_R \frac{\partial \eta}{\partial x} = -\frac{g'}{g} \nabla_h \times \left(\frac{\boldsymbol{\tau}}{\rho_0 f} \right) - \alpha \eta, \tag{1}$$

where η denotes SSH; x and t longitude and time, respectively; $\nabla_h = (\partial_x, \partial_y)$ the horizontal gradient operator; g the acceleration due to gravity; $\boldsymbol{\tau}$ the wind stress vector; $\rho_0 = 1025\,\mathrm{kg\,m^{-3}}$ the mean seawater density; f the Coriolis parameter; c_R phase speed defined to be positive when directed westward; g' reduced gravity; and α the damping coefficient. Equation (1) was integrated at each latitude from the east to the west in the domain from 30° to 120°E using the method of characteristics. Surface wind stresses were obtained from ERA5. Observed SSH anomalies along the west coast of Australia were used as the eastern boundary condition. The period of the integration is from January 1993 to February 2020, for which both of wind stress and SSH data are available. Observed SSH anomalies in January 1993 were used as the initial condition. We regarded the first two years of model time series as a spinup period and excluded them from our analysis. In this study we compare observations and model results and also compare the part of the model solution which is locally driven by winds with the part driven by eastern boundary conditions. The wind-driven part of the solution was obtained by setting SSH anomalies at the eastern boundary to zero. The boundary-driven part was computed by setting $\boldsymbol{\tau} = 0$ in Eq. (1).

There are three free parameters in the model, i.e., c_R, α, and g'. We chose these parameters as follows. It is widely known that zonal phase speeds observed in satellite altimetry are significantly different from theoretically expected phase speed for a linear long Rossby wave in an ocean at rest (Chelton and Schlax 1996). The observed westward phase speed is faster at midlatitudes (roughly poleward of 20°N/S) and slower in tropical regions (equatorward of 20°N/S) compared to theory. This discrepancy can be explained by mean flow effects (Killworth et al. 1997; Dewar 1998; de Szoeke and Chelton 1999), topography (Tailleux and McWilliams 2001) and/or instability due to resonant triad and the generation of barotropic mode (LaCasce and Pedlosky 2004). Considering this discrepancy, we used prescribed values for c_R, as is done in previous studies (Qiu and Chen 2006; Zhuang et al. 2013; Menezes and Vianna 2019). Figure 1a compares the theoretically expected phase speed (red line) with the phase speed for which model results are most highly correlated with observations (black solid line). The theoretical phase speed was computed as $\beta c^2/f^2$ (e.g., Qiu et al. 1997), where c is shallow water gravity wave phase speed and β is the meridional gradient of f. We computed the zonal averages of Brunt–Väisälä frequency

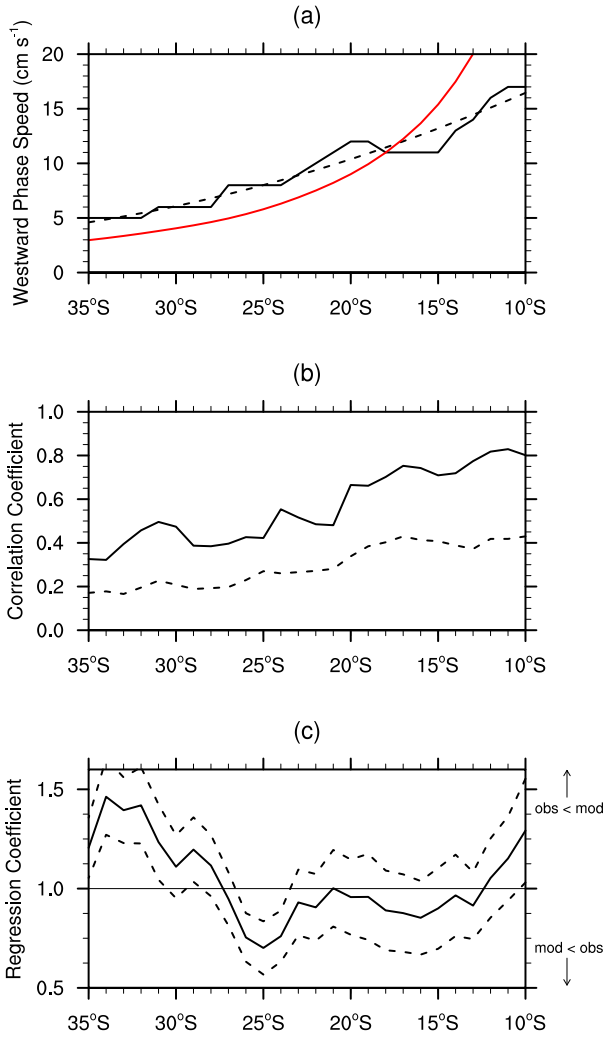

FIG. 1. (a) Estimates of westward phase speed obtained from correlation analysis between satellite altimetry and results from the 1D wave model (black line), and theoretical phase speed for a first baroclinic, long, free Rossby wave in an ocean at rest (red line). The dashed line shows the least squares fit of a quadratic curve onto the black line. (b) Pattern correlation and (c) neutral regression coefficients between satellite observations and model results at each latitude. The dashed line in (b) illustrates the 99% confidence level for correlation coefficients, and that in (c) shows the 95% confidence interval for neutral regression coefficients computed following Garrett and Petrie (1981).

squared between 50° and 110°E from the *World Ocean Atlas 2013* (Locarnini et al. 2013; Zweng et al. 2013) and obtained c by solving the equation $\partial_z \psi_n = -(N^2/c_n^2)\int_{-D}^{z} \psi_n \, dz$ at each latitude, where N^2 denotes Brunt–Väisälä frequency squared, ψ_n the vertical profile of the nth vertical mode, c_n the phase speed for the nth mode, and D (=4000 m) the depth of the ocean. We used the phase speed for the first baroclinic mode as c, i.e., $c = c_1$.

The wave model was integrated with prescribed c_R ranging from 0.02 to 0.2 m s^{-1}, and pattern correlation was computed between model results and satellite observations in longitude–time sections at each latitude for the zonal range from 50° to 110°E and for the period from 1995 to 2020. The phase speed for which the pattern correlation is highest is plotted in Fig. 1a. We used $g' = 0.05$ m s^{-1} and $\alpha^{-1} = 2.5$ years, which produced the best results compared to observations. Sensitivity to these parameters is discussed later in this section.

Theoretical Rossby wave phase speed is about 3 cm s^{-1} at 35°S and about 20 cm s^{-1} at 13°S. The phase speed obtained from the observations–model comparison tends to increase to the north, which is a tendency similar to theoretical estimates. However, the phase speed obtained from the observations–model comparison is smaller than theory at low latitudes and larger at higher latitudes. Previous studies (Chelton and Schlax 1996; Menezes and Vianna 2019) reported a similar discrepancy between phase speed observed in satellite altimetry and theoretical values. Menezes and Vianna (2019) examined propagation speed of SSH using satellite observations in the south Indian Ocean and reported a phase speed of about 3–7 cm s^{-1} between 30° and 35°S and 11–18 cm s^{-1} between 10° and 15°S. The phase speed obtained from the observations–model comparison roughly agrees with their results. We least squares fit a quadratic curve to the phase speed obtained from the observations–model comparison (dashed line in Fig. 1a). The resulting phase speed obtained from the fitted curve was used to integrate the model in this study.

Results obtained from the model run were compared with satellite altimetry in terms of pattern correlation and neutral regression coefficients computed using longitude–time sections of SSH anomalies at each latitude. In contrast to standard regression analysis, neutral regression coefficients are calculated by minimizing the sum of the square distances between the regression line and data points, results of which do not depend on which of two variables is chosen as the independent variable (Emery and Thomson 2004). We computed statistical degrees of freedom for correlation by applying the method of Davis (1976). First, we applied the method in the zonal direction and averaged results temporally. Then, we applied the same method in time and averaged results zonally. The zonal degrees of freedom were multiplied by the temporal degrees of freedom, the results of which were used as the effective degrees of freedom at a particular latitude. We show the 99% confidence level for correlation coefficients, if correlations exceed the 99% level. Otherwise, we use the 95% confidence level. For neutral regression coefficients, we show the 95% confidence intervals computed following Garrett and Petrie (1981).

Correlation between observed and simulated SSH exceeds the 99% confidence level at all latitudes (Fig. 1b). Regression coefficients tend to be smaller than unity between 13° and 27°S and larger than unity north of 12°S and south of about 28°S. However, considering the uncertainties in the estimates, these coefficients are indistinguishable from unity at most latitudes except south of 31°S (Fig. 1c).

The model has two other parameters, i.e., the damping coefficient α and reduced gravity g'. To check the sensitivity to α, we integrated the model with various α, keeping the other parameters the same. Pattern correlation between observed

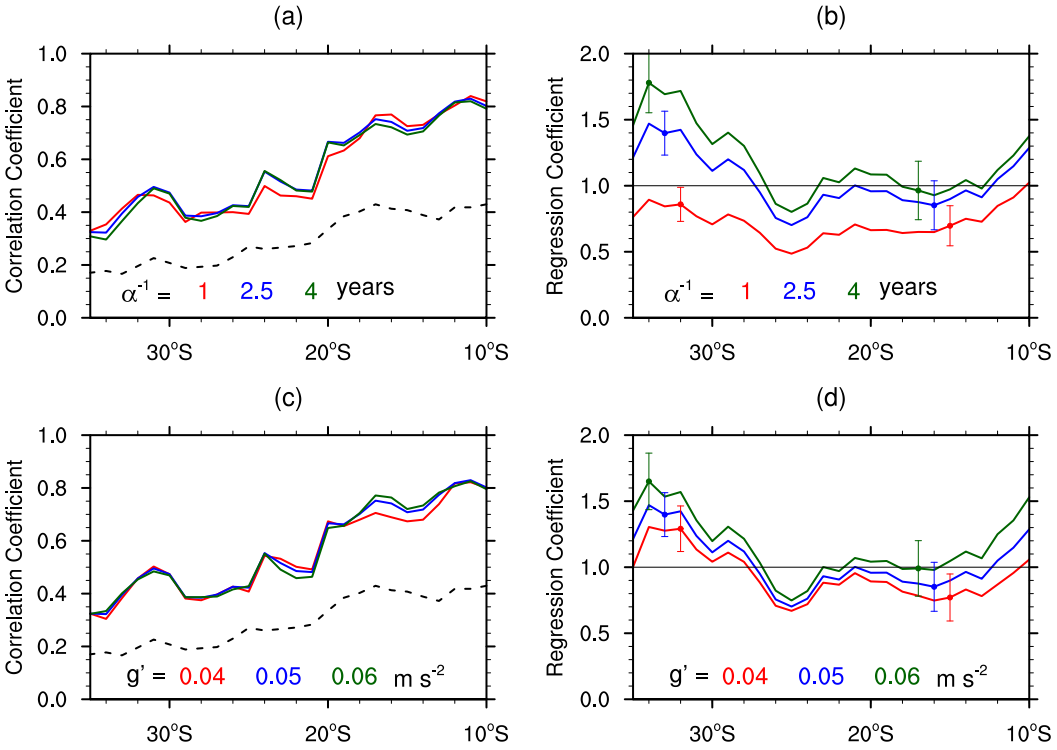

FIG. 2. Sensitivity of model SSH to damping time scale (α^{-1}) and reduced gravity (g'). (a),(c) Pattern correlation coefficients and (b),(d) neutral regression coefficients at each latitude between satellite altimetry measurements and model results. The dashed line in (a) and (c) shows the 99% confidence level for correlation coefficients. Vertical bars in (b) and (d) show the 95% confidence interval for the neutral regression coefficient, which was computed following Garrett and Petrie (1981). Red, blue, and green lines in (a) and (b) show results for $\alpha^{-1} = 1, 2.5$, and 4 years, respectively. Those in (c) and (d) are for results for $g' = 0.04$, 0.05, and 0.06 m s^{-2}, respectively.

and simulated SSH is not sensitive to α (Fig. 2a), whereas model SSH regressed onto observed SSH depends on the choice of α (Fig. 2b). The regression coefficient is about 0.5–1.0 for the run with $\alpha^{-1} = 1$ year, but it is about 0.8–1.8 for the run with $\alpha^{-1} = 4$ years. We also integrated the model with various g', keeping the other parameters fixed. Note that this parameter is included in the coefficient of the forcing term in Eq. (1). If we choose a larger g', the magnitude of wind forcing becomes larger. Results of sensitivity experiments show that pattern correlation between observations and model results is almost the same if we change g' from 0.04 to 0.06 m s^{-2} (Fig. 2c). Model SSH regressed onto observed SSH is larger in the run with a larger g', as expected (Fig. 2d). These results show that α and g' affect only regression coefficients (i.e., the magnitude of simulated variability) but not correlation coefficients (i.e., the spatiotemporal structure). Results also show that the sensitivity to g' varies with respect to latitude. Regressed model SSH is relatively more sensitive to the choice of g' north of 20°S and south of 30°S but less sensitive between 20° and 30°S.

Figure 3 summarizes the sensitivity of pattern regression coefficients to g' and α^{-1}. The regression coefficient tends to be larger in the upper-right part of the diagram and smaller in the lower-left part. The contour line for unit regression coefficient is from the upper left to the lower right of the diagram. The line of the unit regression coefficient is different from latitude to latitude. In this study, we used $g' = 0.05$ m s^{-2} and $\alpha^{-1} = 2.5$ years, for which regression coefficients are close to unity at most latitudes (Figs. 1c and 3). Menezes and Vianna (2019) and Volkov et al. (2020) used $g' = 0.05$ and 0.06 m s^{-2}, respectively, and Zhuang et al. (2013) used $\alpha^{-1} = 3$ yr, which are consistent with our choices.

Our model tuning is based on regression analysis. This approach can be ambiguous, because a combination of a smaller g' and a larger α^{-1} can yield the same regression coefficient as that of a larger g' and a smaller α^{-1} (Fig. 3). Another approach is to tune the model by minimizing the squared differences between observed and simulated SSH (D. Volkov 2020, personal communication). Asterisks in Fig. 3 show the parameters for which the sum of the squared differences at each latitude is minimized. The resulting g' ranges from 0.02 to 0.055 m s^{-2}. The damping time scale α^{-1} chosen by this method ranges from 0.8 to 1.4 years, which is smaller than our choice. Menezes and Vianna (2019) and Volkov et al. (2020) used damping time scales of 1 and 1.3 years, respectively, which are consistent with those obtained from the minimization of squared differences. It is not clear to us which metric, regression analysis or the minimization of squared differences, is optimal for tuning the model. Menezes and Vianna (2019) and Volkov et al. (2020) successfully

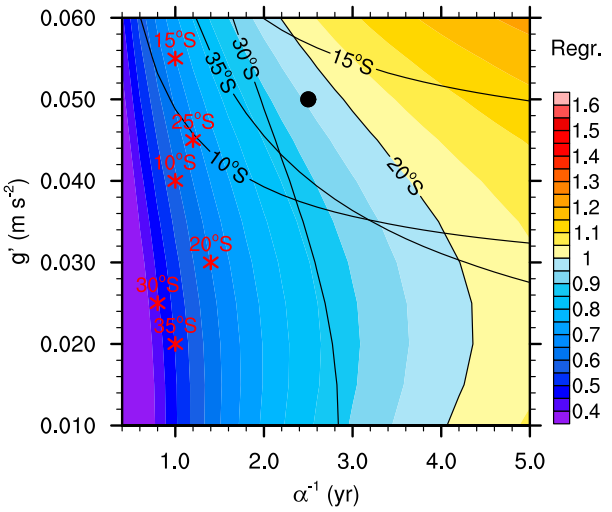

FIG. 3. Neutral regression coefficients between satellite altimetry measurements and model results at each latitude as a function of two model parameters, i.e., reduced gravity (g') and damping time scale (α^{-1}). Color shades show regression coefficients at 20°S. Solid lines show the line on which the regression coefficient is unity. Red asterisks show the values of g' and α^{-1}, for which the squared differences between observations and model results are minimized for 10°–35°S at 5° intervals. The black dot illustrates the parameters used to integrate the model in this study. The line of the unit regression coefficient is shown for 10°, 15°, 20°, 30°, and 35°S, but not for 25°S, because the regression coefficients at 25°S are smaller than unity in the whole parameter domain.

simulated observed variability that they focused on with $\alpha^{-1} = \sim 1$ year. However, if we choose $\alpha^{-1} = 1$ year, the model severely underestimates the amplitude of SSH anomalies compared to observations. In this study, we prioritize accurate simulation of SSH amplitude and for this reason use $\alpha^{-1} = 2.5$ years. We discuss in section 4a that results obtained from Volkov et al.'s (2020) choice of parameters lead to essentially the same conclusions.

In this study, we used $g' = 0.05\,\mathrm{m\,s^{-2}}$ for all the latitudes. Usually, a larger g' is chosen for lower latitudes, and a smaller g' is used for higher latitudes, reflecting the difference in the stratification (e.g., Qiu and Chen 2006; Zhuang et al. 2013). The use of a constant g' can be a reason for the tendency of the overestimation of SSH variability south of 28°S (Fig. 1c). However, it is difficult to tweak this parameter such that modeled SSH anomalies have a similar magnitude to observed SSH anomalies at all latitudes, because modeled SSH anomalies are relatively insensitive to g' between 20° and 30°S (Fig. 2d). Thus, we use $g' = 0.05\,\mathrm{m\,s^{-2}}$ everywhere and confirm that results presented below did not change if we used a slightly different values of g'.

3. Results

In section 3a, we examine zonal and meridional structures of SSH variability. In section 3b, we describe the zonal gradient of SSH anomalies between the western and eastern parts of the basin, which is an index for meridional geostrophic transport of the subtropical gyre. In section 3c, we examine wind forcing in the Indian and Pacific Oceans.

a. SSH variability

First, we describe variability at two latitudes: 13°S (as in Masumoto and Meyers 1998; Fig. 4) and 25°S (as in Menezes and Vianna 2019; Fig. 5). Time series at 13°S indicate SSH anomalies that are mostly negative in the western basin and positive in the eastern basin in 1996–97, 1999–2002, and 2011–13 and positive in the west and negative in the east from 2002 to 2007 (Fig. 4a). Simulated SSH anomalies compare well with these observations (Fig. 4b), although some discrepancies can be found, for example west of 90°E in 2005–06, where observed anomalies are mostly positive but simulated anomalies tend to be negative. In the western part of the model domain, the total solution compares well with the wind-driven part, which shows a predominance of negative anomalies in 2000–03, positive anomalies in 2004–07 and negative anomalies in 2011–13 (Fig. 4c). The boundary-driven part shows positive anomalies in 1999–2003 and 2008–15 and negative anomalies in the other period (Fig. 4d), which consists of anomalies east of about 95°E in the total solution.

At 25°S, observed SSH anomalies tend to be negative from 1995 to 1999, negative east of about 80°E and positive west of 80°E in 2005–09, and mostly positive from 2010 to 2015 (Fig. 5a). Westward propagation of positive SSH anomalies is observed from 1999 to 2002 east of 70°E and from 2011 to 2015 in 50°–110°E. These patterns are well simulated by the model (Fig. 5b), although the linear model does not simulate variability on smaller spatial scales, which are likely due to mesoscale eddies. Observed positive SSH anomalies west of 60°E in 2006–15 tend to be larger in amplitude than anomalies east of 60°E. This amplification is not seen in the model solution, which may be one of the reasons for the underestimate of the amplitude of SSH anomalies by the model near 25°S (Fig. 1c). The boundary-driven part of the model solution (Fig. 5d) tends to be larger in magnitude than the wind-driven part (Fig. 5c) in the central and eastern parts of the basin at this latitude. In the boundary-driven part, positive anomalies propagate to the west from 1999 to 2004 and after 2008, which is also seen in the total solution and observations. The boundary-driven part also shows negative anomalies between 2002 and 2007, which accounts for the dominance of negative anomalies in the eastern basin in this period in the total solution and observations. The wind-driven part shows positive anomalies from 2005 to 2008 in the western part of the basin, which are consistent with observed positive anomalies.

The standard deviations of observed SSH anomalies along 13°S are about 3 to 5 cm (Fig. 6a). The simulated SSH anomalies compare well with the observations, although they tend to be smaller in magnitude than observed. The amplitude of the wind forced part of the model solution increases to the west between 80° and 120°E, which is a consequence of the integration of energy along Rossby wave characteristics. The boundary forced part decays away from the eastern boundary because of damping. The wind forced part is larger in amplitude than the boundary forced solution west of about 94°E, and the opposite is true east of about 94°E.

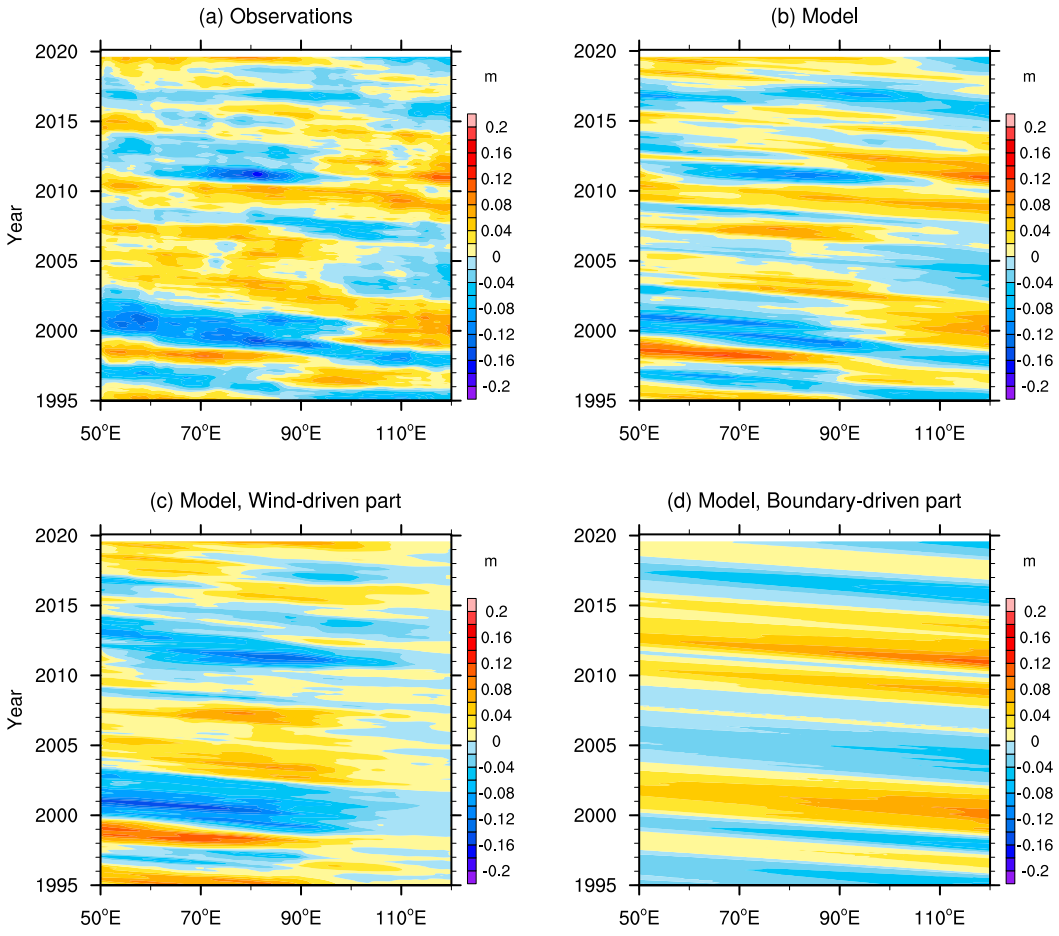

FIG. 4. SSH anomalies at 13°S for (a) observations, (b) model results, (c) the part of the model solution driven by wind forcing, and (d) the part of the model solution driven by eastern boundary conditions. A 13-month running mean was applied to all time series.

Along 25°S, simulated SSH anomalies are much smaller in amplitude than observations west of 90°E (Fig. 6b), which results partly from the lack of amplification near the western boundary (Fig. 5). At this latitude, the boundary forced part is larger than the wind forced part east of 72°E. The region where the boundary forced part is larger is wider at 25°S than at 13°S, which indicates that boundary forcing is more influential in general at 25°S.

Figure 7 shows pattern correlation between observations and the wind-driven part of the model solution (red line) and that between observations and the boundary-driven part (blue line). Correlation with the wind-driven part between 10° and 18°S is higher (and statistically significant at the 99% level) than that with the boundary-driven part (which is not significant at that level). This result reflects the dominance of the wind forced part in the western basin at low latitudes, whereas the boundary forced component is confined to the eastern basin (Fig. 6a). The boundary forced component is larger in amplitude than the wind forced component in the central and eastern basins at midlatitudes (Fig. 6b). Reflecting this, correlation with the boundary-driven part is high and significant between 19° and 33°S. Correlation with the wind-driven part is significant south of 28°S and higher than that with the boundary-driven part between 33° and 35°S. This result shows that local wind forcing makes a larger contribution to the variability at low latitudes, while boundary forcing is more influential at midlatitudes except near 35°S.

b. SSH gradient variability

Zhuang et al. (2013) and Nagura (2020) found that interannual variability in meridional geostrophic transport of the subtropical gyre in the upper 1000 m was proportional to the zonal gradient of SSH anomalies between the western and eastern parts of the south Indian Ocean. Here we focus our SSH analysis on the region between 20° and 35°S, where subtropical gyre transport is northward (e.g., Nagura and McPhaden 2018) and boundary forcing is influential at most latitudes (Fig. 7). The zonal gradient of observed SSH anomalies tends to be in phase meridionally (Fig. 8a). It is negative from 1999 to 2001, positive from 2002 to 2007, negative from 2011 to 2013, and positive in 2015 and 2018–19. These variations are well simulated by the model (Fig. 8b), although linear model results are less noisy due to the lack of mesoscale

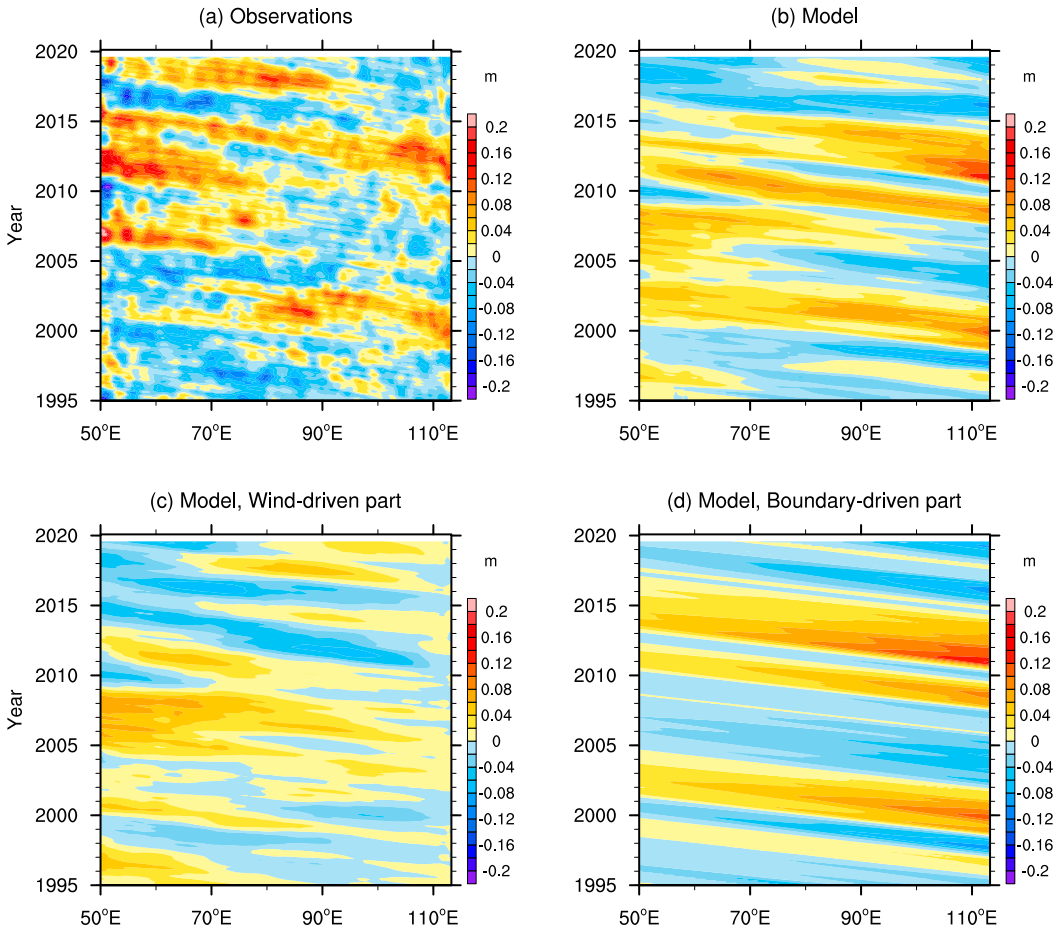

FIG. 5. As in Fig. 4, but for 25°S.

eddies. The zonal SSH gradient anomalies computed from the boundary-driven part (Fig. 8d) compare well with observations and the total solution, which reproduce the characteristics of the time evolution described above. The zonal SSH gradient anomalies obtained from the wind-driven part contribute to positive anomalies in 2005–08 north of 28°S but do not account for negative anomalies in 1999–2001 and 2011–13 (Fig. 8c). Pattern correlation between the observations (Fig. 8a) and the wind-driven part of the solution (Fig. 8c) is 0.02, which is statistically indistinguishable from zero; conversely, correlation between the observations and the boundary forced part of the solution (Fig. 8d) is 0.59, which is significant at the 99% level of confidence.

The amplitude of the zonal difference in observed SSH anomalies tends to be larger at lower latitude and decreases poleward (Fig. 9). The zonal SSH gradient anomalies obtained from the simulation compare well with the observational counterpart, although it underestimates the magnitude of variability between 13° and 25°S and overestimates it south of 26°S. The boundary forced part is larger in magnitude than the wind forced part south of 17°S, which again indicates the large contribution of boundary forcing at midlatitudes. From these results, we conclude that interannual variability in meridional geostrophic transport of the south Indian Ocean is mainly driven by variability at the eastern boundary.

c. *Wind forcing*

The 1D wave model adopted in this study uses observed SSH anomalies as the eastern boundary condition. Menezes and Vianna (2019) showed that observed SSH anomalies are in phase meridionally along the west Australian coast and their amplitude does not change much from 10° to 35°S, which is a consequence of poleward propagation of coastal Kelvin waves. Thus, the magnitude of the eastern boundary forcing does not change much from latitude to latitude in our model. However, the magnitude of wind forcing in the south Indian Ocean is different between low and midlatitudes. Wind stress curl anomalies are large in the area 5°–18°S, 75°–105°E, south of 15°S and west of 80°E, near 40°S, and in the coastal zones (Fig. 10a). Variability is weak in the interior region near the equator and in the region 18°–32°S, 80°–105°E. The magnitude of Ekman pumping velocity anomalies decreases poleward (Fig. 10b), which is expected as Ekman pumping velocity is inversely proportional to the Coriolis coefficient. The amplitude of Ekman pumping velocity anomalies is relatively small in 20°–35°S, 80°–110°E, which roughly coincides with the region

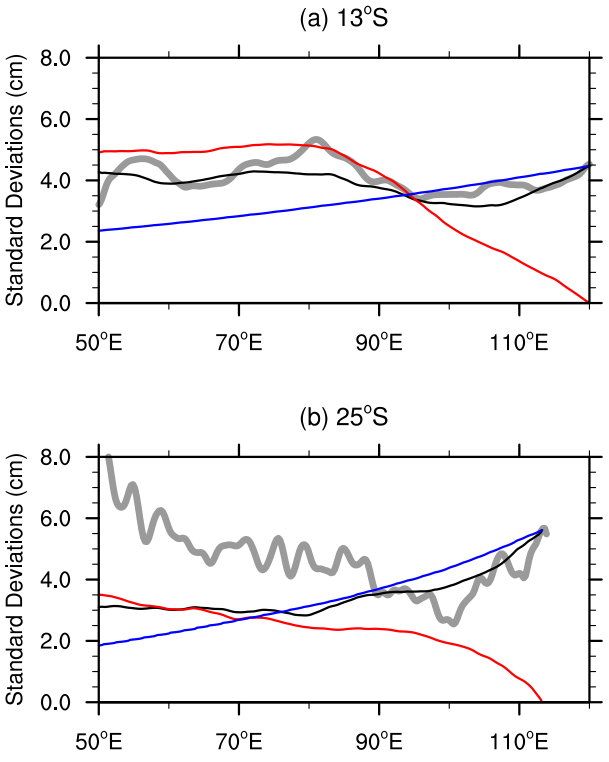

FIG. 6. Standard deviations of observed SSH anomalies (thick gray line), simulated SSH anomalies (black line), the part of the model solution driven by wind forcing (red line), and the part of the model solution driven by eastern boundary conditions (blue line) along (a) 13°S and (b) 25°S.

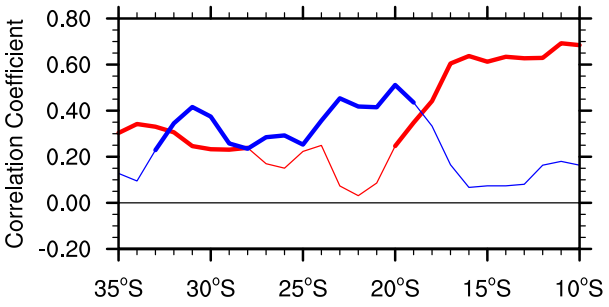

FIG. 7. Pattern correlation coefficients at each latitude between observations and the part of the model solution driven by wind forcing (red line) and between observations and the part of the model solution driven by eastern boundary conditions (blue line). The thick line shows correlation coefficients significant at the 99% confidence level.

with weak wind stress curl anomalies. This shows that the large contribution from eastern boundary forcing at midlatitudes is due to weak wind forcing in the interior ocean.

Previous studies pointed out that SSH variability along the west coast of Australia is caused by variability in tropical Pacific wind forcing (Clarke 1991; Clarke and Liu 1994; Feng et al. 2010, 2011; Menezes and Vianna 2019; Meyers 1996; Potemra 2001; Wijffels and Meyers 2004). We can see this impact of Pacific wind forcing in a comparison of SSH anomaly time series averaged over the southeastern Indian Ocean (SEIO box; 20°–35°S, 105°–115°E) with zonal wind stress anomalies averaged over the equatorial Pacific Ocean (EPO box; 5°S–5°N, 160°E–170°W) and meridional wind stress anomalies averaged over the SEIO (Fig. 11). Note that the EPO box coincides with the region where the amplitude of zonal wind stress anomalies is largest. Zonal wind stress anomalies averaged over this region are highly correlated with multivariate ENSO index (Wolter and Timlin 2011; $r = 0.93$) and closely related to ENSO. Equatorial Pacific wind stress anomalies are also highly correlated with SSH anomalies in the SEIO box (correlation coefficient is −0.83, significant at the 95% level of confidence), with Pacific wind anomalies leading Indian Ocean SSH anomalies by 5 months (Fig. 12a). The simultaneous correlation between SEIO SSH anomalies and local meridional wind stress anomalies is only −0.13 and the lead–lag correlation does not exceed the 95% level of confidence at any lag between ±12 months (Fig. 12b). Wind forcing in the equatorial Indian Ocean excites equatorial Kelvin waves, which are reflected back to the Indian Ocean at the eastern boundary as Rossby waves (Clarke 1991) or propagate into the Indonesian Seas (Durland and Qiu 2003; Wijffels and Meyers 2004) and do not reach the western coast of Australia. Consistently, the correlation between SEIO SSH and zonal wind stress anomalies in the equatorial Indian Ocean (5°S–5°N, 60°–90°E) is not significant at the 95% level at any lag (Fig. 12c).

We computed lead–lag correlation coefficients along the propagation path of SSH anomalies, which connects the western Pacific to the southeastern Indian Ocean (points 1–3 in Fig. 11b). The path in the Pacific Ocean is along 4°N, which is the approximate latitude of SSH variability related to first meridional mode Rossby waves. Clarke (1991) pointed out that the lowest meridional mode of Rossby waves contributes most to variability leaking to the Indian Ocean. It takes about 28 days for a first meridional mode Rossby wave to propagate from point 1 to 2, if the typical value of gravity wave phase speed for the first baroclinic mode is assumed ($2.73\ m\ s^{-1}$; Yu and McPhaden 1999). It takes about 9 days for a coastal Kelvin wave to propagate from point 2 to 3 and from point 3 to the SEIO box. In total therefore, it takes about 28 + 9 + 9 = 46 days for a free wave to propagate from point 1 to the southeastern Indian Ocean. SSH anomalies at point 1 lead those in the SEIO box by 2 months (Fig. 12d), which roughly agrees with the free wave propagation time.

Figure 12e shows the lead–lag correlation between SSH anomalies at point 1 and zonal wind stress anomalies averaged over the EPO box. Zonal wind anomalies lead SSH anomalies by 2 months with a negative correlation. Negative correlation indicates that off-equatorial SSH in the western basin is anomalously depressed when zonal wind anomalies are eastward, and elevated when wind anomalies are westward, which represents a balance between zonal pressure gradient force and zonal wind stress. The explanation for the 2-month time lag is more complicated. Correlation analysis shows that zonal wind stress anomalies are coherent in a region larger than the EPO box (figure not shown), and forced motion is superposed on

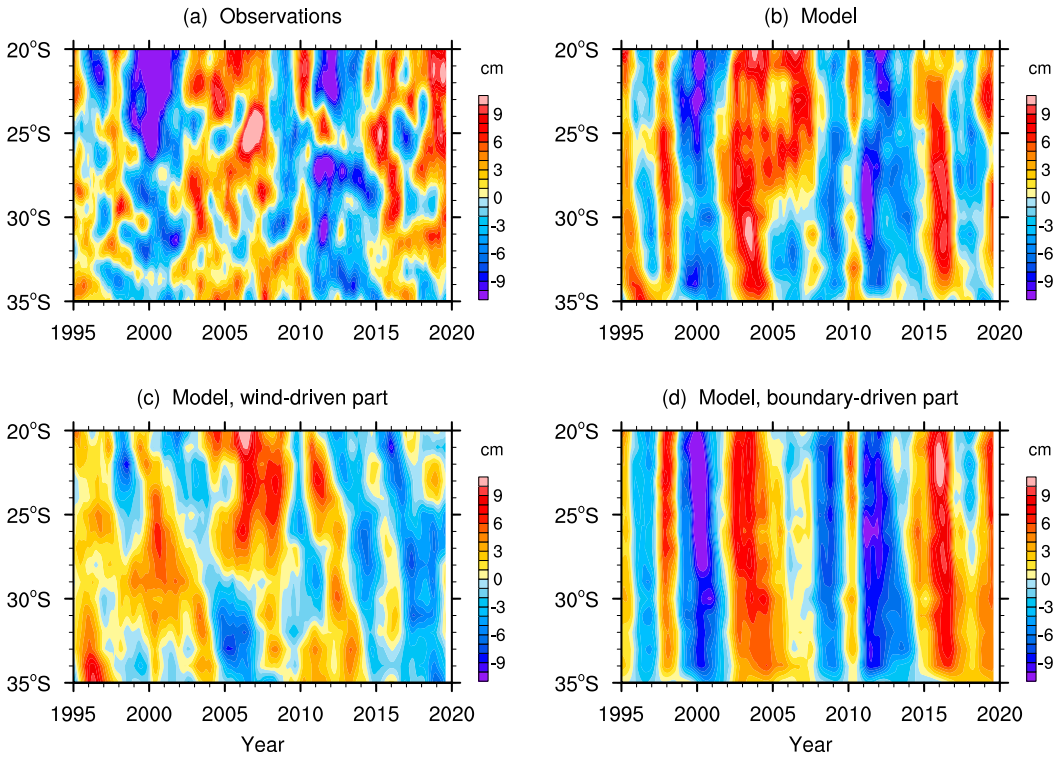

FIG. 8. The zonal difference of SSH anomalies between 50°–60°E and 105°–115°E (former minus latter) as a function of latitude and time for (a) observations, (b) the model solution, (c) the part of the model solution driven by wind forcing, and (d) the part of the model solution driven by eastern boundary conditions. A 13-month running mean was applied to all time series.

propagating waves. The observed 2-month time lag between SSH anomalies at point 1 and zonal wind stress anomalies in the EOP box is a consequence of the superposition of directly forced variability and propagating waves, which we confirmed using a wind-forced linear equatorial wave model. In summary, SSH anomalies in the SEIO box lags SSH anomalies at point 1 by 2 months, and SSH anomalies at point 1 lags zonal wind stress anomalies in the EPO box by 2 months, which roughly

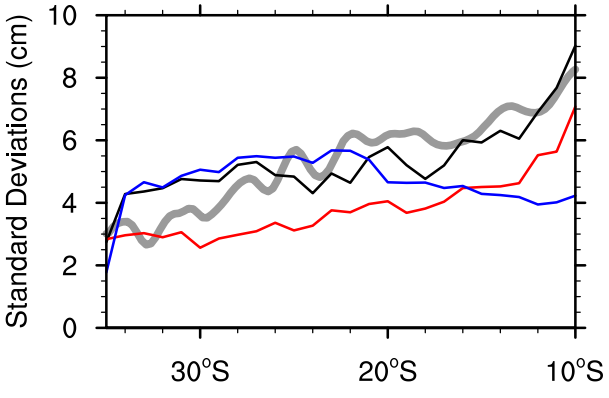

FIG. 9. Standard deviations of the zonal difference of SSH anomalies between 50°–60°E and 105°–115°E (former minus latter) for observed SSH anomalies (thick gray line), simulated SSH anomalies (black line), the part of the model solution driven by wind forcing (red line), and the part of the model solution driven by eastern boundary conditions (blue line) as a function of latitude from 10° to 35°S.

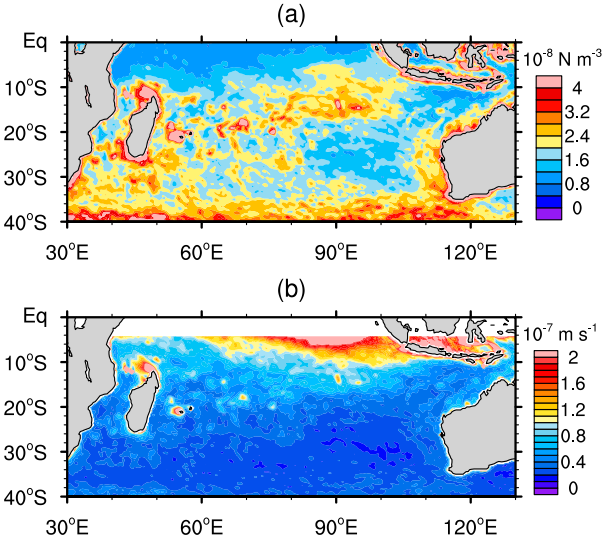

FIG. 10. Standard deviations of (a) wind stress curl and (b) Ekman pumping velocity anomalies. A 13-month running mean was applied before computing standard deviations.

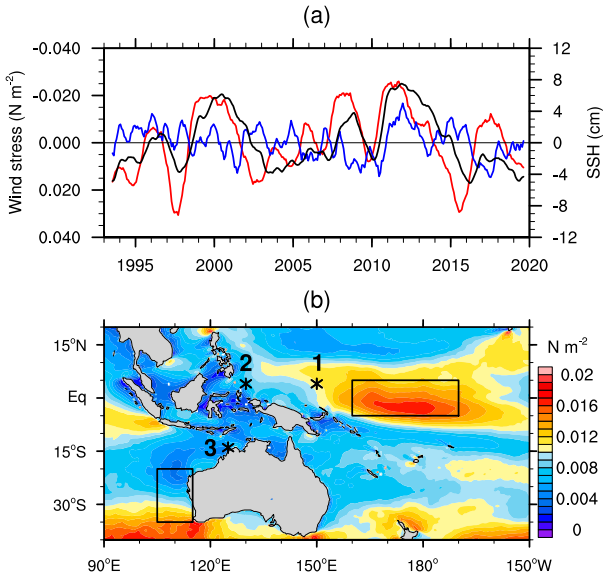

FIG. 11. (a) SSH anomalies averaged over the southeastern Indian Ocean box (SEIO box; 20°–35°S, 105°–115°E; black line), zonal wind stress anomalies averaged over the equatorial Pacific Ocean box (EPO box; 5°S–5°N, 160°E–170°W; red line), and meridional wind stress anomalies averaged over the SEIO box (blue line). A 13-month running mean was applied to the time series. The vertical axis for wind stress anomalies is inverted for ease of comparison with SSH. (b) Standard deviations of zonal wind stress anomalies, with the SEIO box, the EPO box, and points 1 (4°N, 150°E), 2 (4°N, 130°E), and 3 (14°S, 125°E) indicated.

explain the 5 month lag between zonal wind stress anomalies in the EPO box and SSH anomalies in the SEIO box. This confirms that SSH anomalies in the southeastern Indian Ocean originate from zonal wind anomalies in the equatorial Pacific Ocean.

4. Discussion

a. *Results obtained from the model tuned by using least squares differences*

As is described in section 2, we chose the model parameters (α and g') such that regression coefficients between observed and simulated SSH are close to unity. Another method to tune the model is to minimize the squared differences between observations and model results (D. Volkov 2020, personal communication). The largest difference between the two methods is in the choice of α^{-1}, which is 2.5 years in the regression analysis method but about 1 year in the method of the least squared differences. This is owing to the difference in strategy of model tuning and we do not consider that one of the methods is correct and the other is wrong. However, the choice of α^{-1} can be critical, because α^{-1} affects the magnitude of propagating waves and the relative amplitude of wind-forced and boundary-driven components of SSH variability.

To check the sensitivity of our results to these parameters, we integrated Eq. (1) using $\alpha^{-1} = 1.3$ year and $g' = 0.06\,\mathrm{m\,s^{-2}}$, which Volkov et al. (2020) used. We used c_R shown in Fig. 1a in this sensitivity experiment. The solution obtained with Volkov et al.'s parameters is well correlated with observed SSH anomalies (Fig. 13a), but regression coefficients south of 15°S are smaller than those obtained from our standard run (Figs. 1c and 13b), which is due to the use of a short damping time scale. We also find that the amplitude of the wind forced part of the solution increases and the boundary forced part is more tightly trapped near the eastern boundary (Figs. 13c,d). Nevertheless, the boundary forced part is highly correlated with observations at midlatitudes between 19° and 32°S, whereas correlation with the wind forced part is lower than that with the boundary forced part (Fig. 13e). The boundary forced part is also larger in magnitude than the wind forced part between 17° and 34°S in terms of standard deviations of the zonal SSH gradient anomalies (Fig. 13f). This shows that our main conclusion, namely that, in general, the contribution from wind forcing is larger at lower latitudes and the contribution from boundary forcing is larger at midlatitudes, holds if we use Volkov et al.'s parameters.

b. *Relationship with climate modes*

In the previous section, we separated SSH anomalies into the locally forced component and the boundary forced component and attributed the latter to ENSO. However, surface wind anomalies in the south Indian Ocean are also affected by climate modes. There are four climate modes which are influential on south Indian Ocean winds. The first one is ENSO. Volkov et al. (2020) reported that Ekman pumping velocity anomalies north of 35°S are significantly correlated with an ENSO index. The second is the Indian Ocean Dipole (IOD) mode, which is characterized by SST anomalies in the tropical Indian Ocean (Saji et al. 1999; Webster et al. 1999). Saji and Yamagata (2003) reported the impact of IOD on temperature and rainfall in midlatitude regions. The third is the southern annular mode (SAM), which represents variability in sea level pressure over the Antarctic continent and in the surrounding regions (Thompson and Wallace 2000). Gong and Wang (1999), Xue et al. (2004), Lovenduski and Gruber (2005), Ciasto and Thompson (2008), and Ohishi et al. (2015) reported that surface wind anomalies in the south Indian Ocean and variability in the Mascarene High are correlated with a SAM index. The fourth is the subtropical Indian Ocean dipole (SIOD), which is defined as a dipole pattern of SST anomalies in the subtropical region of the south Indian Ocean (Behera and Yamagata 2001). Suzuki et al. (2004) showed that interannual variability in trade winds in the south Indian Ocean is correlated with SIOD.

Here we use zonal wind stress anomalies averaged over the EPO box as an index for ENSO. The IOD index was computed as the difference of SST anomalies between 10°S–10°N, 50°–70°E and 0°–10°S, 90°–110°E, following Saji et al. (1999). The SAM index was obtained from British Antarctic Survey's website (http://www.nerc-bas.ac.uk/icd/gjma/sam.html). The SIOD index was computed as the difference of SST anomalies between 30°–40°S, 50°–70°E and 15°–25°S, 85°–105°E, following Morioka et al. (2012). We used NOAA OI SST to compute the IOD and SIOD indices. These four indices are normalized by their standard deviations. Correlation between the ENSO, SAM, and SIOD indices is not significant, which indicates that

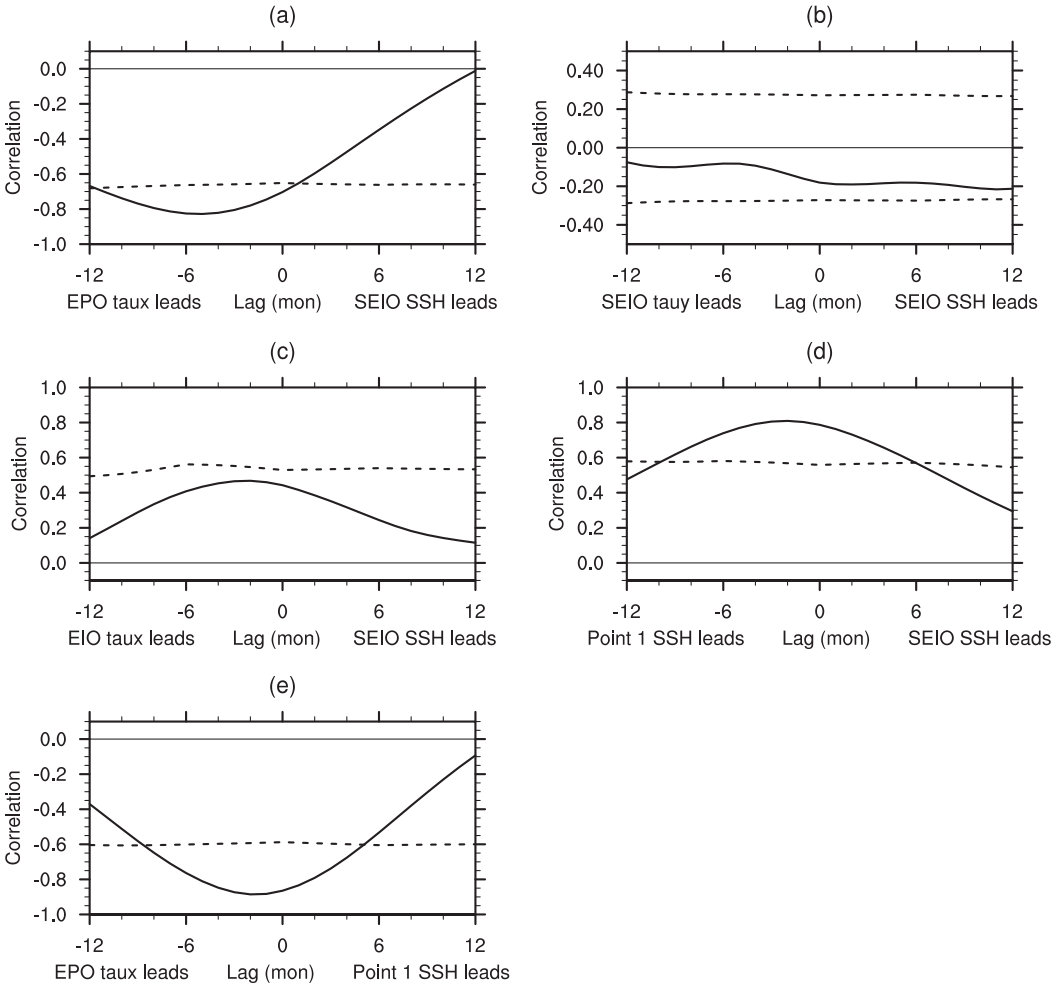

FIG. 12. Lead–lag correlation between (a) SSH anomalies averaged over the SEIO box (20°–35°S, 105°–115°E) and zonal wind stress anomalies averaged over the EPO box (5°S–5°N, 150°E–170°W), (b) SSH anomalies averaged over the SEIO box and meridional wind stress anomalies averaged over the SEIO box, (c) SSH anomalies averaged over the SEIO box and zonal wind stress anomalies averaged over the equatorial Indian Ocean box (5°S–5°N, 60°–90°E), (d) SSH anomalies averaged over the SEIO box and SSH anomalies at point 1 shown in Fig. 11b, and (e) SSH anomalies at point 1 and zonal wind stress anomalies averaged over the EPO box. Dashed line shows the 95% confidence level. A 13-month running mean was applied to all time series before the analysis.

they can be regarded as statistically independent. Correlation between the indices for ENSO and IOD is not significant at the 95% confidence level, which is consistent with results of Saji et al. (1999) and Webster et al. (1999). This is due to that ENSO and IOD events peak in different seasons. Seasonally stratified analysis yields significant correlation between these indices (Allan et al. 2001), which indicates the tendency of co-occurrence of ENSO and IOD events. It is also known that ENSO and IOD affect each other via variability in atmospheric circulations (e.g., Behera et al. 2006; Izumo et al. 2010).

ENSO positively correlated with SLP anomalies in the northeastern part of the south Indian Ocean, which accompany southeastward surface wind anomalies, negative Ekman pumping velocity anomalies north of about 20°S and positive Ekman pumping velocity anomalies between 20° and 35°S (Fig. 14a). These patterns are consistent with results of Yu et al. (2005) and Volkov et al. (2020). IOD is related to positive SLP anomalies in the eastern Indian Ocean and south of Australia, negative Ekman pumping anomalies north of about 15°S and northerly surface wind anomalies between 60° and 100°E (Fig. 14b). The patterns related to IOD are similar to those related to ENSO as is pointed out by Yu et al. (2005), which reflects the tendency of co-occurrence of ENSO and IOD events. The impact of IOD on Ekman pumping velocity at midlatitudes is weaker than that of ENSO, as is pointed out by Volkov et al. (2020). SAM is related to negative SLP anomalies over the Antarctic continent and positive SLP anomalies in the Antarctic Ocean surrounding the continent (e.g., Gong and Wang 1999). SLP regressed to the SAM index shows positive SLP anomalies centered at about 45°S, 100°E and negative SLP anomalies at about 15°S, 95°E (Fig. 14c). The resulting cyclonic circulation leads to positive Ekman pumping velocity

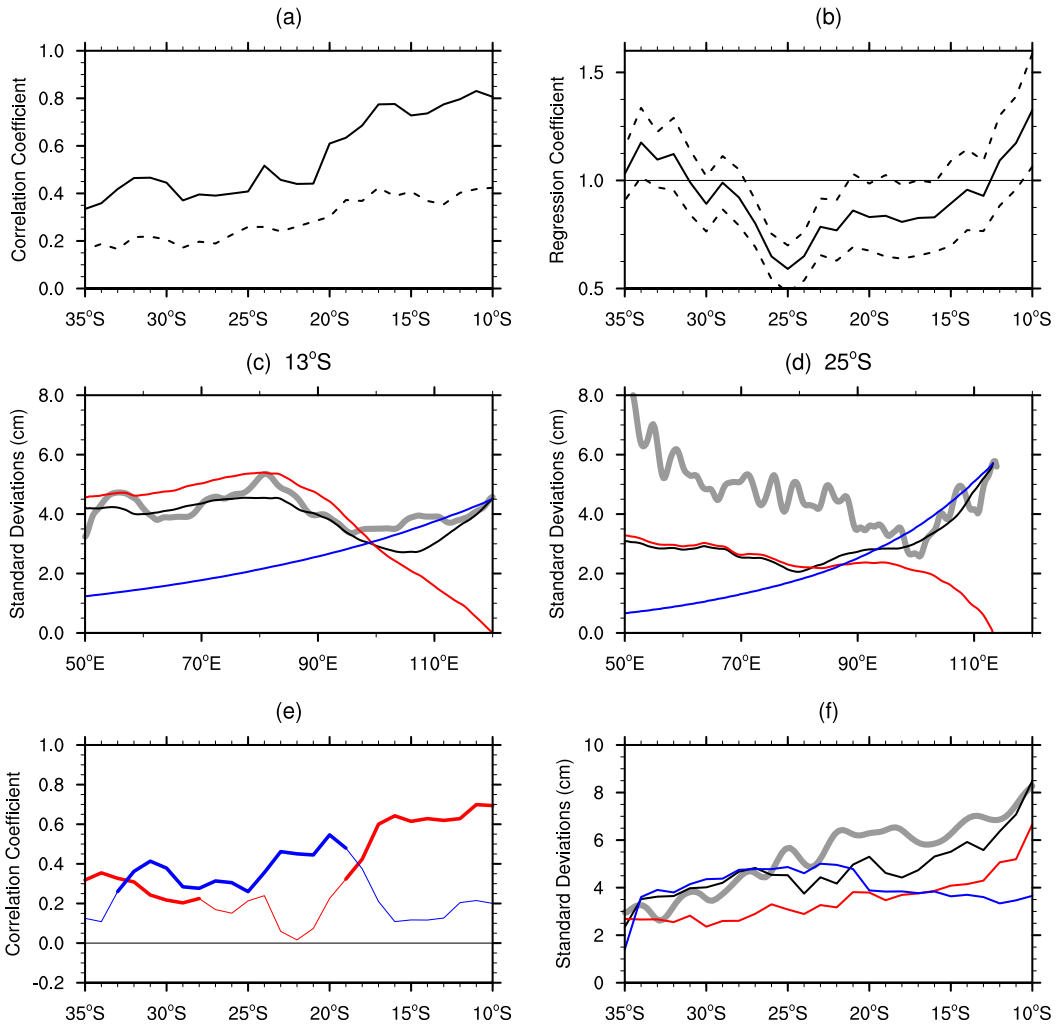

FIG. 13. (a)–(f) As in Figs. 1b, 1c, 6a, 6b, 7, and 9, respectively, but obtained from model results computed with the values of α and g' used in Volkov et al. (2020). In (c)–(f), the red line is for the part of the model solution driven by wind forcing, and the blue line is for the part driven by eastern boundary conditions.

anomalies mainly east of 80°E between 10° and 30°S. SIOD is related to positive SLP anomalies centered at about 30°S, 90°E, which accompany northwestward wind anomalies and negative Ekman pumping velocity anomalies in 20°–30°S, 80°–110°E (Fig. 14d).

These results show that all the four climate modes affect variability in Ekman pumping velocity anomalies at mid-latitudes of the south Indian Ocean. We averaged Ekman pumping velocity anomalies in 20°–35°S and 50°–110°E and computed its linear multiple regression coefficients onto the four climate mode indices. The percent variance explained by the ENSO, IOD, SAM, and SIOD indices is 5%, 4%, 23%, and 9%, respectively. The relatively small contributions from ENSO and IOD are observed in the regression coefficient map in Figs. 14a and 14b, where positive Ekman pumping anomalies are small in amplitude between 20° and 30°S. The variance explained by SIOD is slightly larger than those by ENSO and IOD. Result shows that SAM is the largest contributor to local wind forcing variability in the south Indian Ocean. The four climate modes, in particular SAM, contribute to SSH anomalies in the south Indian Ocean via changes in wind forcing. However, the total percent variance explained by the four climate modes is only 41%, which indicates that the bulk of the variability may result from random atmospheric variability.

5. Summary

This study examines interannual variability in SSH in the south Indian Ocean (10°–35°S), using satellite measurements, an atmospheric reanalysis and a linear, long Rossby wave model. Our focus is on the relative role of wind forcing in the south Indian Ocean versus remote forcing from the equatorial Pacific Ocean. We chose our model parameters–zonal phase speed, the damping coefficient and reduced gravity–by comparing simulated SSH with SSH estimates from satellite altimetry. After parameter tuning, simulated SSH anomalies

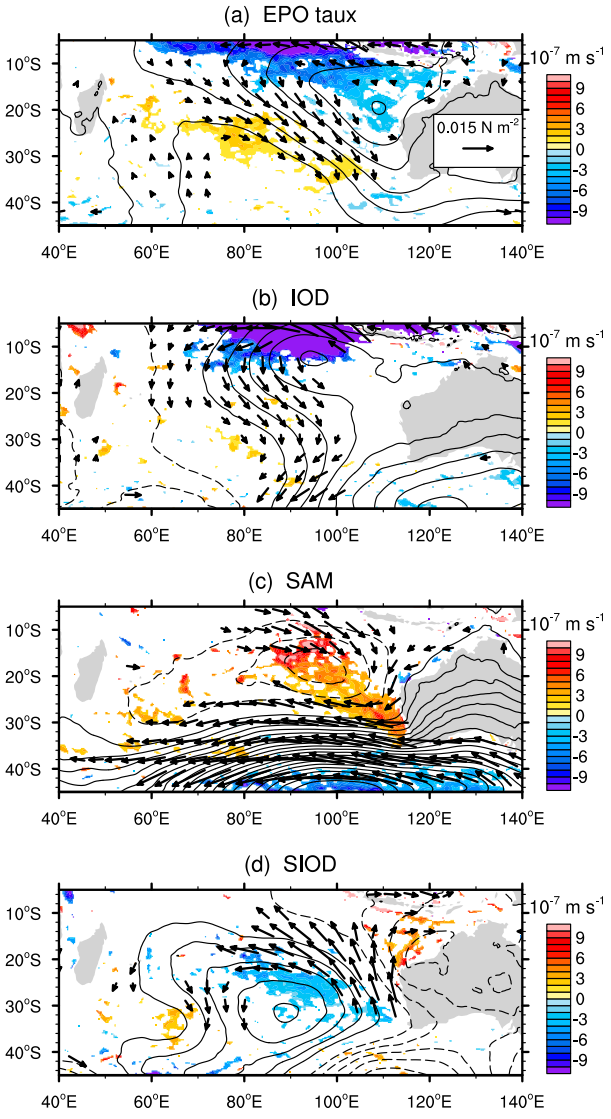

FIG. 14. Ekman pumping velocity anomalies (colors), SLP anomalies (contours), and surface wind stress anomalies (vectors) regressed onto (a) zonal wind stress anomalies averaged over the equatorial Pacific Ocean box (5°S–5°N, 150°E–170°W), (b) the Indian Ocean Dipole index, (c) the southern annular mode index, and (d) the subtropical Indian Ocean dipole index. Regressed Ekman pumping velocity anomalies and surface wind stress anomalies were masked out if they are not significant at the 95% confidence level. Contour intervals are 0.15 hPa. Contours for negative values are shown by dashed lines, and those for zero value were omitted. The scale for regressed surface wind stress anomalies is shown in the top panel. A 13-month running mean was applied to all time series before the analysis.

reproduce the main characteristics of observed SSH anomalies. We decomposed the model solution into the part that is driven locally by winds in the south Indian Ocean and that driven by SSH variability along the west coast of Australia. Results showed that interannual variability in SSH at midlatitudes (between 19° and 33°S) is mainly driven by waves radiated from the west coast of Australia, which originate from wind-driven SSH variability in the tropical Pacific Ocean, rather than local wind forcing, which is weak at midlatitudes. At lower latitudes (between 10° and 18°S), SSH variability in the western basin is mainly driven by local winds and that in the eastern basin is generated by variability radiated from the Australian coast. This highlights the latitudinal dependence of factors causing interannual SSH variability in the south Indian Ocean.

Masumoto and Meyers (1998) and Zhuang et al. (2013) reported the dominance of local wind forcing in driving SSH variability at low latitudes (specifically at 11°–13°S), while Zhuang et al. (2013) and Menezes and Vianna (2019) pointed out the prevalence of variability radiated from the eastern boundary at midlatitudes (20° and 25°S). We have conducted a comprehensive analysis from 10° to 35°S and showed that there are two regimes, one in the tropics where local forcing has a larger effect, and the other at midlatitudes where remote forcing is more influential. Volkov et al. (2020) examined the average of SSH anomalies over 10°–30°S which mixes these two different regimes and so can be misleading. In addition, Volkov et al. used a shorter damping time scale (α^{-1} = 1.3 years) in their long Rossby wave model than ours (α^{-1} = 2.5 years). This difference is caused by different strategies of model tuning, but our main conclusion still holds if we use Volkov et al.'s damping time scale.

An additional analysis shows that ENSO, IOD, SAM, and SIOD are correlated with variability in Ekman pumping velocity in the south Indian Ocean. ENSO and IOD have strong impacts on Ekman pumping velocity anomalies in the tropical region (equatorward of 20°S), but their impact is relatively weak at midlatitudes. Among the four, SAM has the largest impact on Ekman pumping velocity at midlatitudes (23% in variance), whereas those of ENSO, IOD, and SIOD are smaller than that of SAM (5%, 4%, and 9%, respectively). These climate modes can influence SSH anomalies in the south Indian Ocean via their effects on local wind forcing but in aggregate they explain less than half variance in the observed wind field suggesting that much of the wind variations on interannual time scales are random in character.

Our results also show that the zonal gradient of SSH in the south Indian Ocean, which is a measure of meridional geostrophic transport, is primarily driven by variability radiated from the eastern boundary and is thus ultimately forced by winds in the equatorial Pacific Ocean. This indicates that Pacific wind forcing mainly generates variability in subtropical gyre transports of the south Indian Ocean consistent with the hypothesis proposed by Lee and McPhaden (2008). We conclude that the influence from the Pacific Ocean is a critical determinant of the variability in mass and heat transport at midlatitudes of the south Indian Ocean.

Acknowledgments. We thank Denis Volkov for constructive comments on the original version of this manuscript. Comments from an anonymous reviewer are also appreciated. Satellite SSH data and ERA5 data were provided by CMEMS and the Climate Data Store, respectively. NOAA OI SST V2 data were provided by the NOAA/Oceanic and Atmospheric Research/Earth System Research Laboratory

Physical Sciences Laboratory, Boulder, Colorado. This work was supported by JSPS Grants-in-Aid for Scientific Research (KAKENHI) Grant JP18K03750. This is PMEL Contribution Number 5169.

Data availability statement. Satellite SSH data can be downloaded at ftp://my.cmems-du.eu/Core/SEALEVEL_GLO_PHY_L4_REP_OBSERVATIONS_008_047/dataset-duacs-rep-global-merged-allsat-phy-l4. ERA5 data are available at https://cds.climate.copernicus.eu/cdsapp#!/dataset/reanalysis-era5-single-levels-monthly-means?tab=form. NOAA OI SST V2 were obtained at ftp.cdc.noaa.gov/Datasets/noaa.oisst.v2.

REFERENCES

Allan, R., and Coauthors, 2001: Is there an Indian Ocean Dipole, and is it independent of El Niño-southern oscillation? *CLIVAR Exchanges*, Vol. 6, No. 3, International CLIVAR Project Office, Southampton, United Kingdom, 18–22, https://www.clivar.org/sites/default/files/documents/Exchanges21.pdf.

Behera, S. K., and T. Yamagata, 2001: Subtropical SST dipole events in the southern Indian Ocean. *Geophys. Res. Lett.*, **28**, 327–330, https://doi.org/10.1029/2000GL011451.

——, J.-J. Luo, S. Masson, S. A. Rao, and H. Sakuma, 2006: A CGCM study on the interaction between IOD and ENSO. *J. Climate*, **19**, 1688–1705, https://doi.org/10.1175/JCLI3797.1.

Chelton, D. B., and M. G. Schlax, 1996: Global observations of oceanic Rossby waves. *Science*, **272**, 234–238, https://doi.org/10.1126/science.272.5259.234.

Church, J. A., and N. J. White, 2006: A 20th century acceleration in global sea-level rise. *Geophys. Res. Lett.*, **33**, L01602, https://doi.org/10.1029/2005GL024826.

Ciasto, L. M., and D. W. J. Thompson, 2008: Observations of large-scale ocean–atmosphere interaction in the Southern Hemisphere. *J. Climate*, **21**, 1244–1259, https://doi.org/10.1175/2007JCLI1809.1.

Clarke, A.J., 1991: On the reflection and transmission of low-frequency energy at the irregular western Pacific Ocean boundary. *J. Geophys. Res.*, **96**, 3289–3305, https://doi.org/10.1029/90JC00985.

Clarke, A. J., and X. Liu, 1994: Interannual sea level in the northern and eastern Indian Ocean. *J. Phys. Oceanogr.*, **24**, 1224–1235, https://doi.org/10.1175/1520-0485(1994)024<1224:ISLITN>2.0.CO;2.

Davis, R. E., 1976: Predictability of sea surface temperature and sea level pressure anomalies over the North Pacific Ocean. *J. Phys. Oceanogr.*, **6**, 249–266, https://doi.org/10.1175/1520-0485(1976)006<0249:POSSTA>2.0.CO;2.

de Szoeke, R., and D. B. Chelton, 1999: The modification of long planetary waves by homogeneous potential vorticity layers. *J. Phys. Oceanogr.*, **29**, 500–511, https://doi.org/10.1175/1520-0485(1999)029<0500:TMOLPW>2.0.CO;2.

Dewar, W. K., 1998: On "too fast" baroclinic planetary waves in the general circulation. *J. Phys. Oceanogr.*, **28**, 1739–1758, https://doi.org/10.1175/1520-0485(1998)028<1739:OTFBPW>2.0.CO;2.

Ducet, N., P. Y. Le Traon, and G. Reverdin, 2000: Global high-resolution mapping of ocean circulation from TOPEX/Poseidon and ERS-1 and -2. *J. Geophys. Res.*, **105**, 19 477–19 498, https://doi.org/10.1029/2000JC900063.

Durland, T. S., and B. Qiu, 2003: Transmission of subinertial Kelvin waves through a straight. *J. Phys. Oceanogr.*, **33**, 1337–1350, https://doi.org/10.1175/1520-0485(2003)033<1337:TOSKWT>2.0.CO;2.

Emery, W. J., and R. E. Thomson, 2004: Data processing and presentation. *Data Analysis Methods in Physical Oceanography*, W. J. Emery and R. E. Thomson, Eds., Elsevier, 246–249.

Feng, M., M. J. McPhaden, and T. Lee, 2010: Decadal variability of the Pacific subtropical cells and their influence on the southeast Indian Ocean. *Geophys. Res. Lett.*, **37**, L09606, https://doi.org/10.1029/2010GL042796.

——, C. Böning, A. Biastoch, E. Behrens, E. Weller, and Y. Masumoto, 2011: The reversal of the multidecadal trends of the equatorial Pacific easterly winds, and the Indonesian Throughflow and Leeuwin Current transports. *Geophys. Res. Lett.*, **38**, L11604, https://doi.org/10.1029/2011GL047291.

——, M. J. McPhaden, S.-P. Xie, and J. Hafner, 2013: La Niña forces unprecedented Leeuwin Current warming in 2011. *Sci. Rep.*, **3**, 1277, https://doi.org/10.1038/srep01277.

Garrett, C., and B. Petrie, 1981: Dynamical aspects of the flow through the Strait of Belle Isle. *J. Phys. Oceanogr.*, **11**, 376–393, https://doi.org/10.1175/1520-0485(1981)011<0376:DAOTFT>2.0.CO;2.

Gong, D., and S. Wang, 1999: Definition of Antarctic oscillation index. *Geophys. Res. Lett.*, **26**, 459–462, https://doi.org/10.1029/1999GL900003.

Han, W., J. Vialard, M. J. McPhaden, T. Lee, Y. Masumoto, M. Feng, and W. P. M. de Ruijter, 2014: Indian ocean decadal variability: A review. *Bull. Amer. Meteor. Soc.*, **95**, 1679–1703, https://doi.org/10.1175/BAMS-D-13-00028.1.

Hersbach, H., and Coauthors, 2020: The ERA5 global reanalysis. *Quart. J. Roy. Meteor. Soc.*, **146**, 1999–2049, https://doi.org/10.1002/qj.3803.

Izumo, T., and Coauthors, 2010: Influence of the state of the Indian Ocean dipole on the following year's El Niño. *Nat. Geosci.*, **3**, 168–172, https://doi.org/10.1038/ngeo760.

Kataoka, T., T. Tozuka, S. Behera, and T. Yamagata, 2014: On the Ningaloo Niño/Niña. *Climate Dyn.*, **43**, 1463–1482, https://doi.org/10.1007/s00382-013-1961-z.

Killworth, P. D., D. B. Chelton, and R. A. de Szoeke, 1997: The speed of observed and theoretical long extratropical planetary waves. *J. Phys. Oceanogr.*, **27**, 1946–1966, https://doi.org/10.1175/1520-0485(1997)027<1946:TSOOAT>2.0.CO;2.

LaCasce, J. H., and J. Pedlosky, 2004: The instability of Rossby basin modes and the oceanic eddy field. *J. Phys. Oceanogr.*, **34**, 2027–2041, https://doi.org/10.1175/1520-0485(2004)034<2027:TIORBM>2.0.CO;2.

Lee, S.-K., W. Park, M. O. Baringer, A. L. Gordon, B. Huber, and Y. Liu, 2015: Pacific origin of the abrupt increase in Indian Ocean heat content during the warming hiatus. *Nat. Geosci.*, **8**, 445–449, https://doi.org/10.1038/ngeo2438.

Lee, T., 2004: Decadal weakening of the shallow overturning circulation in the South Indian Ocean. *Geophys. Res. Lett.*, **31**, L18305, https://doi.org/10.1029/2004GL020884.

——, and M. J. McPhaden, 2008: Decadal phase change in large-scale sea level and winds in the Indo-Pacific region at the end of the 20th century. *Geophys. Res. Lett.*, **35**, L01605, https://doi.org/10.1029/2007GL032419.

Locarnini, R. A., and Coauthors, 2013: *Temperature*. Vol. 1, *World Ocean Atlas 2013*. NOAA Atlas NESDIS 73, 40 pp., http://data.nodc.noaa.gov/woa/WOA13/DOC/woa13_vol1.pdf.

Lovenduski, N. S., and N. Gruber, 2005: Impact of the southern annular mode on southern ocean circulation and biology. *Geophys. Res. Lett.*, **32**, L11603, https://doi.org/10.1029/2005GL022727.

Masumoto, Y., and G. Meyers, 1998: Forced Rossby waves in the southern tropical Indian Ocean. *J. Geophys. Res.*, **103**, 27 589–27 602, https://doi.org/10.1029/98JC02546.

Menezes, V. V., and M. L. Vianna, 2019: Quasi-biennial Rossby and Kelvin waves in the south Indian ocean: Tropical and subtropical modes and the Indian Ocean Dipole. *Deep-Sea Res. II*, **166**, 43–63, https://doi.org/10.1016/j.dsr2.2019.05.002.

Meyers, G., 1996: Variation of Indonesian throughflow and El Niño-Southern Oscillation. *J. Geophys. Res.*, **101**, 12 255–12 263, https://doi.org/10.1029/95JC03729.

Morioka, Y., T. Tozuka, S. Masson, P. Terray, J.-J. Luo, and T. Yamagata, 2012: Subtropical dipole modes simulated in a coupled general circulation model. *J. Climate*, **25**, 4029–4047, https://doi.org/10.1175/JCLI-D-11-00396.1.

Nagura, M., 2020: Variability in meridional transport of the subtropical circulation in the south Indian Ocean for the period from 2006 to 2017. *J. Geophys. Res. Oceans*, **124**, e2019JC015874, https://doi.org/10.1029/2019JC015874.

——, and M. J. McPhaden, 2018: The shallow overturning circulation in the Indian Ocean. *J. Phys. Oceanogr.*, **48**, 413–434, https://doi.org/10.1175/JPO-D-17-0127.1.

Nieves, V., J. K. Willis, and W. C. Patzert, 2015: Recent hiatus caused by decadal shift in Indo-Pacific heating. *Science*, **349**, 532–535, https://doi.org/10.1126/science.aaa4521.

Ohishi, S., S. Sugimoto, and K. Hanawa, 2015: Zonal movement of the Mascarene High in austral summer. *Climate Dyn.*, **45**, 1739–1745, https://doi.org/10.1007/s00382-014-2427-7.

Potemra, J. T., 2001: Contribution of equatorial Pacific winds to southern tropical Indian Ocean Rossby waves. *J. Geophys. Res.*, **106**, 2407–2422, https://doi.org/10.1029/1999JC000031.

Qiu, B., and S. Chen, 2006: Decadal variability in the large-scale sea surface height field of the South Pacific Ocean: Observations and causes. *J. Phys. Oceanogr.*, **36**, 1751–1762, https://doi.org/10.1175/JPO2943.1.

——, W. Miao, and P. Müller, 1997: Propagation and decay of forced and free baroclinic Rossby waves in off-equatorial oceans. *J. Phys. Oceanogr.*, **27**, 2405–2417, https://doi.org/10.1175/1520-0485(1997)027<2405:PADOFA>2.0.CO;2.

Reynolds, R. W., N. A. Rayner, T. M. Smith, D. C. Stokes, and W. Wang, 2002: An improved in situ and satellite SST analysis for climate. *J. Climate*, **15**, 1609–1625, https://doi.org/10.1175/1520-0442(2002)015<1609:AIISAS>2.0.CO;2.

Saji, N. H., and T. Yamagata, 2003: Possible impacts of Indian Ocean Dipole mode events on global climate. *Climate Res.*, **25**, 151–169, https://doi.org/10.3354/cr025151.

——, B. N. Goswami, P. N. Vinayachandran, and T. Yamagata, 1999: A dipole mode in the tropical Indian Ocean. *Nature*, **401**, 360–363, https://doi.org/10.1038/43854.

Stramma, L., and J. R. E. Lutjeharms, 1997: The flow field of the subtropical gyre of the south Indian Ocean. *J. Geophys. Res.*, **102**, 5513–5530, https://doi.org/10.1029/96JC03455.

Suzuki, R., S. K. Behera, S. Iizuka, and T. Yamagata, 2004: Indian Ocean subtropical dipole simulated using a coupled general circulation model. *J. Geophys. Res.*, **109**, C09001, https://doi.org/10.1029/2003JC001974.

Tailleux, R., and J. C. McWilliams, 2001: Bottom pressure decoupling and the speed of extratropical baroclinic Rossby waves. *J. Phys. Oceanogr.*, **31**, 1461–1476, https://doi.org/10.1175/1520-0485(2001)031<1461:TEOBPD>2.0.CO;2.

Thompson, D. W. J., and J. M. Wallace, 2000: Annular modes in the extratropical circulation. Part I: Month-to-month variability. *J. Climate*, **13**, 1000–1016, https://doi.org/10.1175/1520-0442(2000)013<1000:AMITEC>2.0.CO;2.

Trenary, L. L., and W. Han, 2008: Causes of decadal subsurface cooling in the tropical Indian Ocean during 1961–2000. *Geophys. Res. Lett.*, **35**, L17602, https://doi.org/10.1029/2008GL034687.

Vialard, J., 2015: Hiatus heat in the Indian ocean. *Nat. Geosci.*, **8**, 423–424, https://doi.org/10.1038/ngeo2442.

Volkov, D. L., S.-K. Lee, A. L. Gordon, and M. Rudko, 2020: Unprecedented reduction and quick recovery of the South Indian Ocean heat content and sea level in 2014-2018. *Sci. Adv.*, **6**, eabc1151, https://doi.org/10.1126/sciadv.abc1151.

Webster, P. J., A. M. Moore, J. P. Loschnigg, and R. R. Leben, 1999: Coupled ocean–atmosphere dynamics in the Indian Ocean during 1997–98. *Nature*, **401**, 356–360, https://doi.org/10.1038/43848.

Wijffels, S., and G. Meyers, 2004: An intersection of oceanic waveguides: Variability in the Indonesian throughflow region. *J. Phys. Oceanogr.*, **34**, 1232–1253, https://doi.org/10.1175/1520-0485(2004)034<1232:AIOOWV>2.0.CO;2.

Wolter, K., and M. S. Timlin, 2011: El Niño/Southern Oscillation behaviour since 1871 as diagnosed in an extended multivariate ENSO index (MEI.ext). *Int. J. Climatol.*, **31**, 1074–1087, https://doi.org/10.1002/joc.2336.

Xue, F., H. Wang, and J. He, 2004: Interannual variability of Mascarene high and Australian high and their influences on east Asian summer monsoon. *J. Meteor. Soc. Japan*, **82**, 1173–1186, https://doi.org/10.2151/jmsj.2004.1173.

Yu, W., B. Xiang, L. Liu, and N. Liu, 2005: Understanding the origins of interannual thermocline variations in the tropical Indian Ocean. *Geophys. Res. Lett.*, **32**, L24706, https://doi.org/10.1029/2005GL024327.

Yu, X., and M. J. McPhaden, 1999: Seasonal variability in the equatorial Pacific. *J. Phys. Oceanogr.*, **29**, 925–947, https://doi.org/10.1175/1520-0485(1999)029<0925:SVITEP>2.0.CO;2.

Zhuang, W., M. Feng, Y. Du, A. Schiller, and D. Wang, 2013: Low-frequency sea level variability in the southern Indian Ocean and its impacts on the oceanic meridional transports. *J. Geophys. Res. Oceans*, **118**, 1302–1315, https://doi.org/10.1002/jgrc.20129.

Zweng, M. M., and Coauthors, 2013: *Salinity*. Vol. 2, *World Ocean Atlas 2013*, NOAA Atlas NESDIS 74, 39 pp., http://data.nodc.noaa.gov/woa/WOA13/DOC/woa13_vol2.pdf.